

# Kinetic Parameter Estimation from Attenuated SPECT Projection Measurements<sup>1</sup>

BW Reutter<sup>†</sup>, *Member, IEEE*; GT Gullberg<sup>‡</sup>, *Senior Member, IEEE*;  
and RH Huesman<sup>†</sup>, *Senior Member, IEEE*

<sup>†</sup> Center for Functional Imaging, Lawrence Berkeley National Laboratory  
University of California, Berkeley, CA 94720, USA

<sup>‡</sup> Department of Radiology, University of Utah, Salt Lake City, UT 84132, USA

## Abstract

Conventional analysis of dynamically acquired nuclear medicine data involves fitting kinetic models to time-activity curves generated from regions of interest defined on a temporal sequence of reconstructed images. However, images reconstructed from the inconsistent projections of a time-varying distribution of radiopharmaceutical acquired by a rotating SPECT system can contain artifacts that lead to biases in the estimated kinetic parameters. To overcome this problem we investigated the estimation of kinetic parameters directly from projection data by modeling the data acquisition process. To accomplish this it was necessary to parametrize the spatial and temporal distribution of the radiopharmaceutical within the SPECT field of view.

In a simulated transverse slice, kinetic parameters were estimated for simple one compartment models for three myocardial regions of interest, as well as for the liver. Myocardial uptake and washout parameters estimated by conventional analysis of noiseless simulated data had biases ranging between 1–63%. Parameters estimated directly from the noiseless projection data were unbiased as expected, since the model used for fitting was faithful to the simulation. Predicted uncertainties (standard deviations) of the parameters obtained for 500,000 detected events ranged between 2–31% for the myocardial uptake parameters and 2–23% for the myocardial washout parameters.

## I. INTRODUCTION

Conventional analysis of dynamically acquired nuclear medicine data involves fitting kinetic models to time-activity curves generated from regions of interest (ROIs) defined on a temporal sequence of reconstructed images. Since dynamic single photon emission computed tomography (SPECT) data acquisition involves gantry motion and the distribution of radiopharmaceutical changes during the acquisition, projections at different angles come from different tracer distributions. Images reconstructed from these inconsistent projections can contain artifacts that lead to biases in the estimated kinetic parameters. The artifacts can be particularly problematic in images reconstructed from projections acquired during the early time frames of a dynamic study when the

tracer distribution is changing most rapidly (Figure 1).

To overcome this problem we investigated the estimation of kinetic parameters directly from projection data by modeling the data acquisition process of a time-varying distribution of radiopharmaceutical detected by a rotating SPECT system. To accomplish this it was necessary to parametrize the spatial and temporal distribution of the radiopharmaceutical within the SPECT field of view.

This approach is potentially useful for clinical studies, particularly in those clinics which have only single detector SPECT systems and thus are not able to perform rapid tomographic acquisitions. Even with a three-detector system, a patient study that utilizes body contouring orbits can take 45–60 sec to obtain one full tomographic acquisition. Thus, the estimation of kinetic parameters directly from projection data may be useful even for multi-detector SPECT systems in some cases.

Direct estimation of kinetic parameters from projections has become an active area of research. Chiao et al. [1, 2] have jointly estimated myocardial ROI boundaries and one-compartment kinetic model parameters directly from simulated positron emission tomography (PET) projections. Limber et al. [3] have fit single decaying exponentials to each pixel in a 16×16 array directly from simulated SPECT projections. We have fit one-compartment models to ROIs encompassing a 3×3 array directly from simulated SPECT projections, by first estimating the exponential factors using linear time-invariant system theory and then estimating the multiplicative coefficients using linear estimation [4].

Estimation of ROI time-activity curves from projections has been investigated. Huesman [5] has described a method to estimate the average activity in a 2-D ROI, and Defrise et al. [6] have extended these ideas to 3-D. To compensate for physical factors such as attenuation and detector resolution, Carson [7] has described a method for estimating activity densities assumed to be uniform in a set of ROIs using maximum likelihood, and Formiconi [8] has similarly used least squares.

The work presented here builds on the work of Carson and Formiconi, as well as on simulations which we have performed in 2-D and 3-D using idealized non-attenuating phantoms [4, 9, 10]. In this 2-D simulation we use the more realistic mathematical cardiac torso (MCAT) phantom [11] and include the effects of attenuation. We compare the estimation of kinetic parameters directly from projections with estimation from tomographic determination of time-activity curves, for three myocardial ROIs and for the liver.

<sup>1</sup>This work was supported by U.S. Department of Health and Human Services grants R01-HL50663 and P01-HL25840 and by U.S. Department of Energy contract DE-AC03-76SF00098.

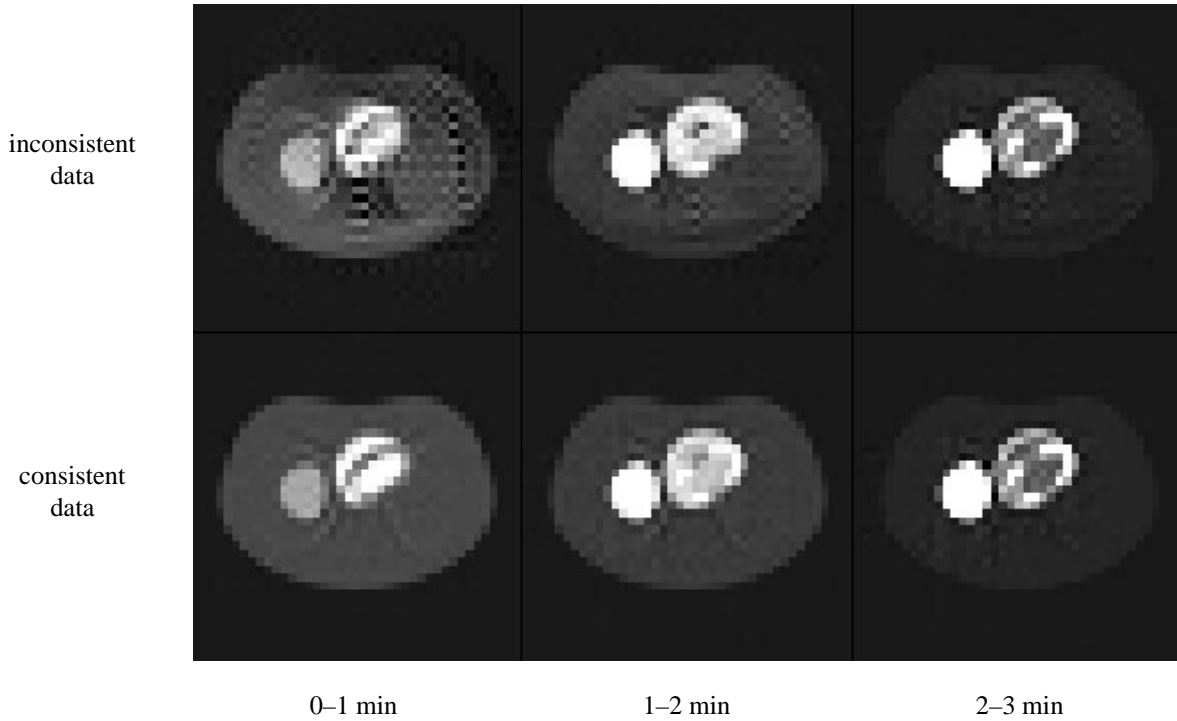


Fig. 1 Artifacts are apparent in the upper sequence of images reconstructed from the inconsistent projections of a relatively rapidly changing tracer distribution acquired during the early uptake and washout time frames of a simulated dynamic SPECT study. The lower sequence of images is obtained when the tracer distribution does not change during the time frames.

## II. ESTIMATION OF KINETIC PARAMETERS DIRECTLY FROM PROJECTIONS

We formulate a nonlinear estimation problem using a spatial and temporal parametrization of the time-varying distribution measured with a single rotating detector SPECT system. The one-compartment model shown in Figure 2 is assumed for simulated myocardial and liver tissue with a known blood input function, which would correspond to the kinetics of teboroxime [12, 13, 14]. Parameters are estimated by minimizing a weighted sum of squared differences between the projections and the model predicted values.

The expression for uptake in tissue type  $m$  is

$$Q^m(t) = k_{21}^m \int_0^t B(\tau) e^{-k_{12}^m(t-\tau)} d\tau = k_{21}^m V^m(t), \quad (1)$$

where  $B(t)$  is the known blood input function,  $k_{21}^m$  is the uptake

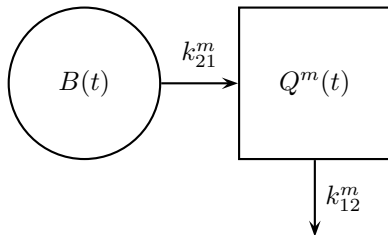


Fig. 2 Compartmental model for  $^{99m}\text{Tc}$ -teboroxime in the myocardium.

parameter, and  $k_{12}^m$  is the washout parameter. Total activity in the tissue is given by

$$Q^m(t) + f_v^m B(t) = k_{21}^m V^m(t) + f_v^m B(t), \quad (2)$$

where  $f_v^m$  is the fraction of vasculature in the tissue.<sup>2</sup>

This analysis starts with an image in which all volume elements (voxels) within the body are segmented into blood pool,  $M$  tissue types of interest, and background. In order to obtain tissue boundaries, the patient is assumed motionless during data acquisition, and a reconstructed image (for example, via the projections at the time of strongest signal, or via the summed projections) is segmented to provide anatomical structure. The image intensity at each segmented region is not used. Each voxel outside the body is modeled to have zero activity concentration (even if its reconstructed image intensity is non-zero) and therefore does not contribute events to the modeled projections. Similarly, a voxel within the body thought to have zero activity concentration could be modeled as such by not labeling the voxel as either blood pool, one of the  $M$  tissue types of interest, or background.

Using the segmented image and a measured attenuation distribution, the attenuated static projections of the blood

<sup>2</sup>Total tissue activity is often modeled as  $(1 - f_v^m)k'_{21}^m V^m(t) + f_v^m B(t)$ . This model yields the identical solution as equation (2), i.e., the same modeled projections are obtained when the weighted sum of squared differences between the measured and the modeled projections is minimized. The relationship between  $k'_{21}^m$  and  $k_{21}^m$  is  $k'_{21}^m = k_{21}^m / (1 - f_v^m)$ .

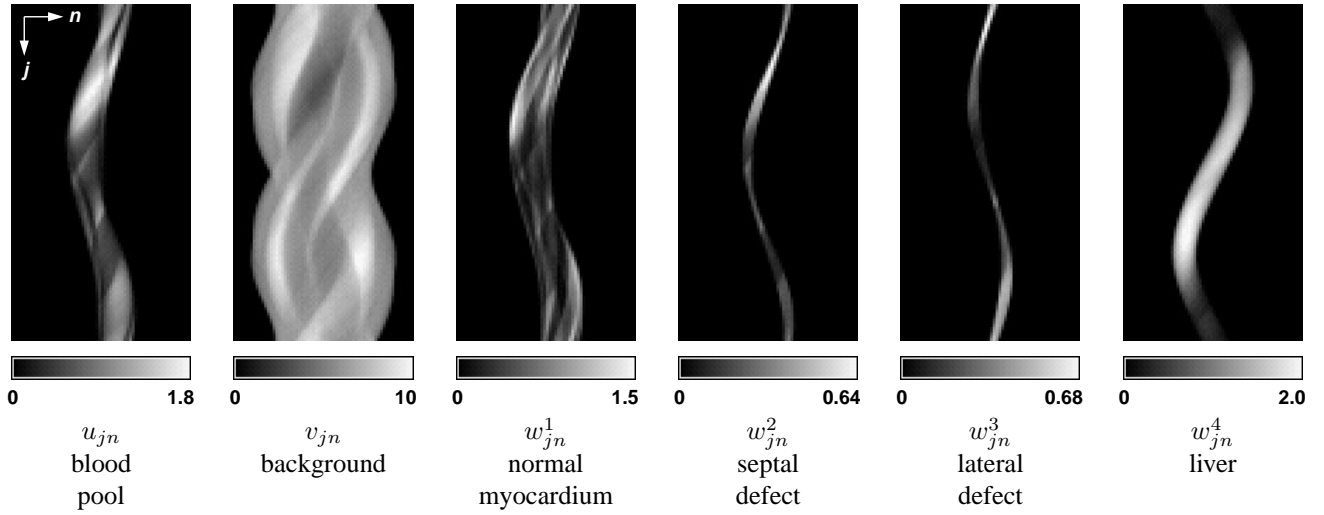


Fig. 3 Attenuated static projections of the ROIs in the MCAT phantom shown in Figures 4 and 5. These are the sinograms that would be observed for each region, given a static unit concentration of activity within the region.

pool, tissue, and background regions are calculated for each projection ray of each projection angle. These are the sinograms that would be observed for each region, given a static unit concentration of activity within the region. With no attenuation, the static projections correspond to the lengths of the blood pool, tissue, and background regions along each projection ray of each projection angle. When projecting the regions, other physical factors such as scatter and geometric point response can be modeled, although we have not done so in this simulation.

The number of projection rays per projection angle is denoted by  $N$ , the number of projection angles per gamma camera rotation by  $J$ , and the number of gamma camera rotations by  $I$ . Thus, there are a total of  $I \cdot J \cdot N$  projection rays distributed in time and space. For a typical projection ray at angle  $j$  and position  $n$ , the attenuated static projections of the blood pool, background, and tissue  $m$  are denoted by  $u_{jn}$ ,  $v_{jn}$ , and  $w_{jn}^m$ , respectively. Figure 3 shows the attenuated static projections of the ROIs in the MCAT phantom (Figures 4 and 5) used in the computer simulations described in Section III. The amplitude of the background activity is denoted by  $g$ , and the background is assumed to be proportional to the blood activity. The projection equations can be expressed as

$$p_{ijn} = \int_{t_{ij}-\Delta t}^{t_{ij}} \left\{ u_{jn}B(\tau) + v_{jn}gB(\tau) + \sum_{m=1}^M w_{jn}^m [k_{21}^m V^m(\tau) + f_v^m B(\tau)] \right\} d\tau, \quad (3)$$

where the time  $t_{ij}$  is equal to  $[j + (i - 1)J]\Delta t$ . The constants  $u_{jn}$ ,  $v_{jn}$ , and  $w_{jn}^m$  are pure geometrical weighting factors, and the projection equations are linear in the unknowns  $g$ ,  $k_{21}^m$ , and  $f_v^m$ . The nonlinear parameters,  $k_{12}^m$ , are contained in  $V^m(t)$ .

The criterion which is minimized by varying the model

parameters is the weighted sum of squares function

$$\chi^2 = \sum_{i=1}^I \sum_{j=1}^J \sum_{n=1}^N \frac{(p_{ijn}^* - p_{ijn})^2}{W_{ijn}}, \quad (4)$$

where  $p_{ijn}^*$  are the measured data and  $W_{ijn}$  are weighting factors. Typically, the weighting factors are either unity for an unweighted fit, or the estimated variances of the projections for a weighted fit.

As discussed above, equation (3) is a linear function of the parameters  $g$ ,  $k_{21}^m$ , and  $f_v^m$ . Therefore the model it describes is called a conditionally linear, partially linear, or separable nonlinear model [15, 16]. We now describe the technique that we have used to remove the conditionally linear parameters so that equation (4) can be considered to be a function of only the nonlinear washout parameters,  $k_{12}^m$ .

The washout parameters are denoted by the vector

$$\lambda = [k_{12}^1 \cdots k_{12}^M]^T \quad (5)$$

and the multiplicative parameters by the vector

$$\mu = [g \ k_{21}^1 \cdots k_{21}^M \ f_v^1 \cdots f_v^M]^T. \quad (6)$$

During the time interval from  $t_{ij} - \Delta t$  to  $t_{ij}$  (corresponding to the  $j$ th projection angle acquired during the  $i$ th rotation), the attenuated static projections of the blood pool, background, and tissue type  $m$  along each of the  $N$  projection rays are denoted by the vectors

$$\mathbf{u}_{ij} = [u_{j1} \cdots u_{jN}]^T, \quad (7)$$

$$\mathbf{v}_{ij} = [v_{j1} \cdots v_{jN}]^T, \quad (8)$$

$$\mathbf{w}_{ij}^m = [w_{j1}^m \cdots w_{jN}^m]^T, \quad (9)$$

respectively. The modeled values for the projections acquired during this time interval are denoted by the vector

$$\mathbf{p}_{ij} = [p_{ij1} \cdots p_{ijN}]^T \quad (10)$$

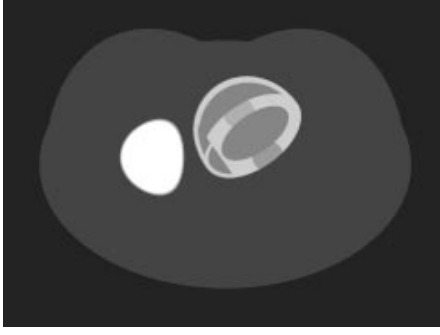


Fig. 4 MCAT emission phantom used in simulation.



Fig. 5 MCAT attenuation phantom used in simulation.

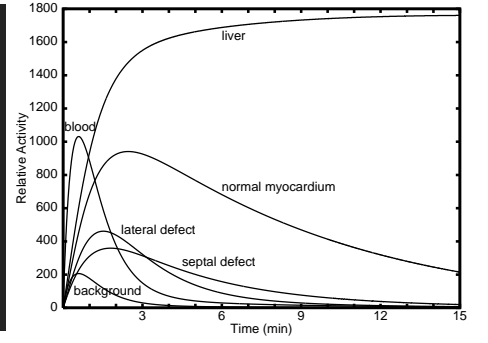


Fig. 6 Simulated time-activity curves for regions of interest.

and the entire set of  $I \cdot J \cdot N$  modeled projections is denoted by the vector

$$\mathbf{p} = [\mathbf{p}_{11}^T \quad \cdots \quad \mathbf{p}_{1J}^T \quad \cdots \quad \mathbf{p}_{I1}^T \quad \cdots \quad \mathbf{p}_{IJ}^T]^T. \quad (11)$$

The corresponding entire set of measured projections is denoted by the vector  $\mathbf{p}^*$ .

Equation (3) can now be written as the set of  $I \cdot J \cdot N$  equations

$$\mathbf{R}\boldsymbol{\mu} = \tilde{\mathbf{p}}, \quad (12)$$

where

$$\mathbf{R} = \begin{bmatrix} \mathbf{v}_{11}B_{11} & \mathbf{w}_{11}^1V_{11}^1 & \cdots & \mathbf{w}_{11}^M V_{11}^M & \mathbf{w}_{11}^1B_{11} & \cdots & \mathbf{w}_{11}^M B_{11} \\ \vdots & \vdots & & \vdots & \vdots & & \vdots \\ \mathbf{v}_{1J}B_{1J} & \mathbf{w}_{1J}^1V_{1J}^1 & \cdots & \mathbf{w}_{1J}^M V_{1J}^M & \mathbf{w}_{1J}^1B_{1J} & \cdots & \mathbf{w}_{1J}^M B_{1J} \\ \vdots & \vdots & & \vdots & \vdots & & \vdots \\ \mathbf{v}_{I1}B_{I1} & \mathbf{w}_{I1}^1V_{I1}^1 & \cdots & \mathbf{w}_{I1}^M V_{I1}^M & \mathbf{w}_{I1}^1B_{I1} & \cdots & \mathbf{w}_{I1}^M B_{I1} \\ \vdots & \vdots & & \vdots & \vdots & & \vdots \\ \mathbf{v}_{IJ}B_{IJ} & \mathbf{w}_{IJ}^1V_{IJ}^1 & \cdots & \mathbf{w}_{IJ}^M V_{IJ}^M & \mathbf{w}_{IJ}^1B_{IJ} & \cdots & \mathbf{w}_{IJ}^M B_{IJ} \end{bmatrix} \quad (13)$$

and

$$\tilde{\mathbf{p}} = \mathbf{p} - \begin{bmatrix} \mathbf{u}_{11}B_{11} \\ \vdots \\ \mathbf{u}_{1J}B_{1J} \\ \vdots \\ \mathbf{u}_{I1}B_{I1} \\ \vdots \\ \mathbf{u}_{IJ}B_{IJ} \end{bmatrix}. \quad (14)$$

The corresponding entire set of measured projections with modeled blood pool contributions subtracted is denoted by the vector  $\tilde{\mathbf{p}}^*$ . In equations (13) and (14),  $B_{ij}$  and  $V_{ij}^m$  are time integrals of the known blood input function and the modeled shape of the tissue  $m$  time-activity curve defined in equation (1), respectively:

$$B_{ij} = \int_{t_{ij}-\Delta t}^{t_{ij}} B(\tau) d\tau, \quad (15)$$

$$\begin{aligned} V_{ij}^m &= \int_{t_{ij}-\Delta t}^{t_{ij}} V^m(\tau) d\tau \\ &= \int_{t_{ij}-\Delta t}^{t_{ij}} \left[ \int_0^\tau B(\tau') e^{-k_{12}^m(\tau-\tau')} d\tau' \right] d\tau. \end{aligned} \quad (16)$$

Equation (4) can now be written as

$$\chi^2 = (\tilde{\mathbf{p}}^* - \mathbf{R}\boldsymbol{\mu})^T \mathbf{W} (\tilde{\mathbf{p}}^* - \mathbf{R}\boldsymbol{\mu}), \quad (17)$$

where  $\mathbf{W}$  is a diagonal matrix with the reciprocals of the weighting factors  $W_{ijn}$  along the diagonal. Given the blood input function  $B(t)$  and values for the washout parameters  $\boldsymbol{\lambda}$ , the criterion  $\chi^2$  is minimized by the multiplicative parameters

$$\boldsymbol{\mu} = (\mathbf{R}^T \mathbf{W} \mathbf{R})^{-1} \mathbf{R}^T \mathbf{W} \tilde{\mathbf{p}}^*. \quad (18)$$

Substituting equation (18) into (17), the criterion  $\chi^2$  can be written as

$$\chi^2 = \tilde{\mathbf{p}}^{*T} \mathbf{W} \tilde{\mathbf{p}}^* - \tilde{\mathbf{p}}^{*T} \mathbf{W} \mathbf{R} (\mathbf{R}^T \mathbf{W} \mathbf{R})^{-1} \mathbf{R}^T \mathbf{W} \tilde{\mathbf{p}}^*, \quad (19)$$

where now the criterion  $\chi^2$  depends only on the washout parameters  $\boldsymbol{\lambda}$  that enter nonlinearly via the matrix  $\mathbf{R}$ . To optimize a fit based explicitly on all of the model parameters, the form of equation (17) can be used.

The covariance matrix for the resulting model parameter estimates  $\hat{\boldsymbol{\Theta}} = [\hat{\boldsymbol{\lambda}}^T \quad \hat{\boldsymbol{\mu}}^T]^T$  is

$$\text{cov}(\hat{\boldsymbol{\Theta}}) = (\mathbf{M}^T \mathbf{W} \mathbf{M})^{-1} \mathbf{M}^T \mathbf{W} \text{cov}(\mathbf{p}^*) \mathbf{W} \mathbf{M} (\mathbf{M}^T \mathbf{W} \mathbf{M})^{-1}, \quad (20)$$

where  $\text{cov}(\mathbf{p}^*)$  is the covariance matrix for the measured projections and the matrix  $\mathbf{M}$  contains the partial derivatives of the modeled projections with respect to the model parameters, evaluated at  $\hat{\boldsymbol{\Theta}}$ :

$$\mathbf{M} = \left. \frac{\partial \mathbf{p}}{\partial \boldsymbol{\Theta}} \right|_{\boldsymbol{\Theta}=\hat{\boldsymbol{\Theta}}}. \quad (21)$$

Given an estimate of  $\text{cov}(\mathbf{p}^*)$ , estimates of the statistical uncertainties of the parameter estimates  $\hat{\boldsymbol{\Theta}}$  are the square roots

		noiseless inconsistent data					noiseless consistent data	
		(a) simulated	(b) conventional	(c) Formiconi	(d) direct	(e) direct uncertainty	(b') conventional	(c') Formiconi
normal myocardium	$k_{21}^1$	0.700	0.665	0.767	0.700	0.010	0.669	0.700
	$k_{12}^1$	0.150	0.149	0.162	0.150	0.002	0.152	0.150
	$f_v^1$	0.150	0.160	-0.032	0.150	0.023	0.187	0.150
septal defect	$k_{21}^2$	0.300	0.112	0.314	0.300	0.074	0.291	0.300
	$k_{12}^2$	0.300	0.116	0.286	0.300	0.065	0.279	0.300
	$f_v^2$	0.100	0.394	0.110	0.100	0.105	0.134	0.100
lateral defect	$k_{21}^3$	0.500	0.218	0.096	0.500	0.151	0.480	0.500
	$k_{12}^3$	0.600	0.247	0.214	0.600	0.133	0.467	0.600
	$f_v^3$	0.100	0.278	0.199	0.100	0.131	0.137	0.100
liver	$k_{21}^4$	0.900	0.924	0.888	0.900	0.005	0.923	0.900
	$k_{12}^4$	0.0020	0.0020	0.0006	0.0020	0.0007	0.0020	0.0020
	$f_v^4$	0.200	0.236	0.325	0.200	0.013	0.198	0.200
background	$g$	0.200	0.200	0.201	0.200	0.001	0.199	0.200

Table 1

Results of kinetic parameter estimation from noiseless inconsistent projections: (a) simulated values; (b) values from dynamic reconstructions; (c) values from direct estimation of region time-activity curves [8]; (d) values from direct estimation from projections; (e) predicted uncertainties (standard deviations) of values from unweighted direct estimation for 500,000 detected events using equation (20). Results of kinetic parameter estimation from noiseless consistent projections: (b') values from dynamic reconstructions; (c') values from direct estimation of region time-activity curves [8]. Units for uptake  $k_{21}^m$  and washout  $k_{12}^m$  are  $\text{min}^{-1}$ , and the vascular fraction  $f_v^m$  and background amplitude  $g$  are dimensionless.

of the diagonal elements of the covariance matrix given by equation (20).<sup>3</sup>

### III. COMPUTER SIMULATIONS

A transverse slice of the MCAT phantom was used in a simulation to evaluate the ability to estimate kinetic parameters directly from attenuated SPECT projection data. The simulated emission distribution, shown in Figure 4, contained blood, background, liver, and three myocardial regions of interest (normal myocardium, septal defect, and lateral defect). The emission distribution was assumed to be attenuated using the attenuation distribution shown in Figure 5, calculated for 140 keV. The attenuation coefficients were  $0.16 \text{ cm}^{-1}$  for soft tissue,  $0.14 \text{ cm}^{-1}$  for breast,  $0.045 \text{ cm}^{-1}$  for lung,  $0.21 \text{ cm}^{-1}$  for rib and transverse processes of spine, and  $0.17 \text{ cm}^{-1}$  for vertebral body. The blood input function and the simulated tissue activity curves are shown in Figure 6.

There were 13 parameters to estimate: the amplitudes, washout rates, and vascular fractions for the liver and the three myocardial regions and the amplitude of the overall background. Using these 13 parameters, the known blood input function, and the known segmentation of the MCAT phantom, a dynamic sinogram was formed representing the attenuated projections of the six constituent components (blood, background, liver, normal myocardium, septal defect,

lateral defect), which comprise the image volume. The 15 min data acquisition protocol consisted of 15 revolutions of a single-head SPECT system, acquiring 120 angles per revolution and 64 parallel projection samples per angle. The projection bin width was 7 mm. Neither scatter nor geometric point response were included in the simulation.

The four washout parameters were estimated by minimizing the unweighted sum of squared differences between the noiseless simulated projection data and the model predicted values given by equation (19), using a modified iterative Newton-Raphson optimization algorithm [15, 16]. In equation (19), the vector  $\tilde{\mathbf{p}}^*$  contained 115,200 measured projections with modeled blood pool contributions subtracted, the weighting matrix  $\mathbf{W}$  was an identity matrix, and the matrix  $\mathbf{R}$  had dimensions  $115,200 \times 9$ . The washout parameters entered nonlinearly via columns 2–5 of the matrix  $\mathbf{R}$ . Starting with all of the washout parameters at zero, it took 10 iterations to converge to the parameter values used to simulate the projections. Each unweighted fit iteration took 2.0 min on a 150 MHz MIPS R10000-based Silicon Graphics O2 workstation.

The results of the noiseless simulation are shown in Table 1 and Figure 7. Direct parameter estimation from noiseless inconsistent projections (column d of Table 1) was compared with estimation from dynamic reconstructions (column b). Fifteen  $41 \times 41$  attenuation corrected reconstructions (one for each 1 min time frame) were formed by using 30 iterations of the conjugate gradient algorithm [18]. Thirty iterations were sufficient to assure that the reconstructions had converged. Line-length weighting was used in the formulation of the projections. The reconstructed pixel dimensions were 1.5 times

<sup>3</sup>The variance of the uptake parameter  $\hat{k}'_{21} = \hat{k}_{21}^m / (1 - \hat{f}_v^m)$  discussed in footnote 2 can be estimated as follows [17]:

$$\frac{\text{var}(\hat{k}'_{21})}{(\hat{k}'_{21})^2} = \frac{\text{var}(\hat{k}_{21}^m)}{(\hat{k}_{21}^m)^2} + \frac{\text{var}(\hat{f}_v^m)}{(1 - \hat{f}_v^m)^2} - \frac{2\text{cov}(\hat{k}_{21}^m, \hat{f}_v^m)}{\hat{k}_{21}^m(1 - \hat{f}_v^m)}.$$

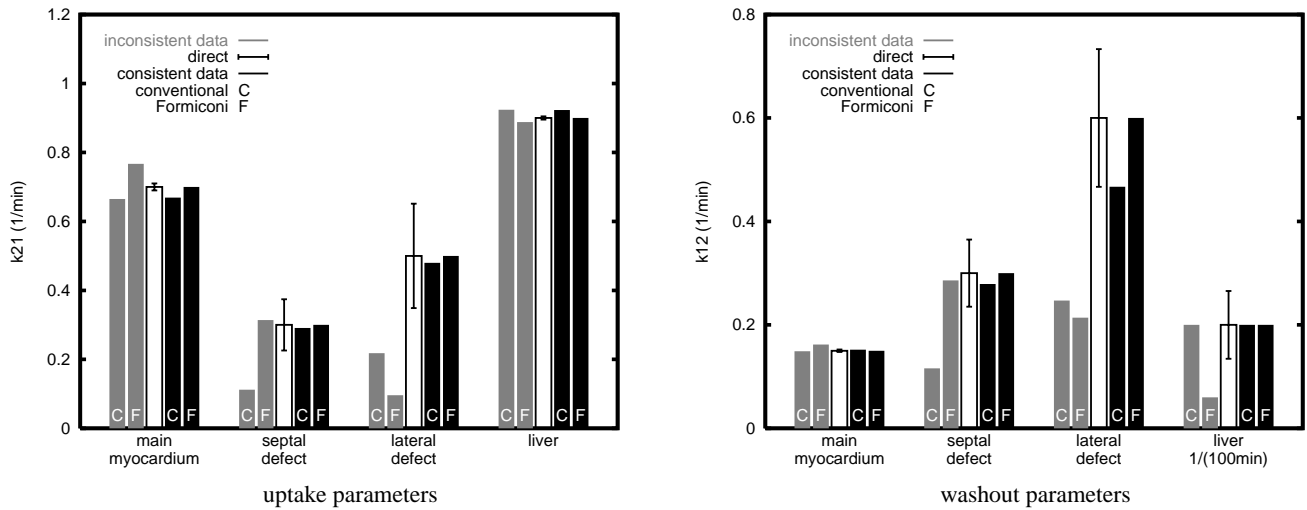


Fig. 7 Estimated values for the uptake parameters  $k_{21}^m$  (left) and the washout parameters  $k_{12}^m$  (right). The gray bars depict the estimates obtained from conventional and Formiconi analyses of noiseless inconsistent projections (columns b and c in Table 1). The white bar depicts the unbiased estimate (i.e., the simulated value) obtained directly from the projections, along with its predicted uncertainty (standard deviation) for an unweighted fit of 500,000 detected events using equation (20). The black bars depict the estimates obtained from conventional and Formiconi analyses of noiseless consistent projections (columns b' and c'). Note that the units for the liver washout parameter,  $k_{12}^4$ , are  $(100 \text{ min})^{-1}$ .

the projection bin width (i.e.,  $10.5 \times 10.5 \text{ mm}$ ). Images reconstructed from the noiseless inconsistent projections for the first three time frames are shown in the upper sequence of Figure 1. ROIs were defined by taking all homogeneous blood pool, background, and liver pixels, as well as all pixels containing at least 90% of one of the three myocardial tissue types. Direct parameter estimation from projections was also compared to the direct estimation of region time-activity curves (column c) using the method proposed by Formiconi [8].

Parameter estimates obtained from conventional analysis of noiseless inconsistent projections had biases ranging between 5–63% for the myocardial uptake parameters and 1–61% for the myocardial wash-out parameters. The large biases in the septal and lateral defects are not unexpected considering the long tomographic acquisition times of 1 min. The estimates using Formiconi's method had less bias in the septal defect and more bias in the normal myocardium and the lateral defect, compared to the conventional method.

The difference in bias between the conventional and Formiconi methods was due to the differing nature of the artifacts in the dynamic image reconstructions and the directly estimated time-activity curves. Both contained artifacts due to the inconsistent projections, because the image reconstruction and the direct time-activity curve estimation are based on a temporal model in which the activity concentrations are constant during the course of each revolution of the SPECT system. The image reconstructions contained additional artifacts (even with temporally consistent projections) due to the limited resolution of the voxels used to model the field of view. The Formiconi method, however, used a spatial model for fitting which was faithful to the simulation.

Parameters estimated directly from the noiseless projection data were unbiased as expected, since both the temporal and

spatial models used for fitting were faithful to the simulation. The uncertainties (standard deviations) of the parameters obtained from an unweighted fit of 500,000 detected events were predicted using equation (20) with an identity matrix for the weighting matrix  $\mathbf{W}$ . The predicted uncertainties (column e) ranged between 2–31% for the myocardial uptake parameters and 2–23% for the myocardial washout parameters. To assess the potential improvement in kinetic parameter precision resulting from a weighted fit based on the estimated covariance of the projection data, the inverse of the known covariance matrix for the simulated projections was also used as the weighting matrix  $\mathbf{W}$  in equation (20). For 500,000 detected events this reduced the average predicted variance of the estimated parameters by about 30% for the myocardial uptake parameters and about 40% for the myocardial washout parameters.

Parameter estimates were also obtained from noiseless projections forced to be consistent over the 1 min time frame of the simulated dynamic data acquisition. Over the course of each revolution of the SPECT system, the activity in each region was held constant at the average of the continuously varying value that yielded the inconsistent projections. Images reconstructed from the noiseless consistent projections for the first three time frames are shown in the lower sequence of Figure 1. For the conventional analysis the biases changed very little for the main myocardium and were reduced substantially for the septal and lateral defects (column b'). The estimates obtained using Formiconi's method were unbiased for the forced consistent projections as expected (column c'), since now both the temporal and spatial models used for fitting were faithful to the simulation.

Lastly, noisy projection data sets containing 250,000, 500,000, and 1 million detected events were simulated.

Multiple local minima were not encountered regardless of count level, when performing an unweighted fit starting with all of the washout parameters at zero or at the values used to simulate the projections.

#### IV. SUMMARY

The combination of gantry motion and the time-variation of the radiopharmaceutical distribution being imaged results in inconsistent projection data sets. Estimating kinetic parameters from time-activity curves taken from reconstructed images results in biases. Some of these biases are reduced and some are increased if the time-activity curves are estimated from the projection data [8]. Estimating the kinetic parameters directly from the projections removes all bias for faithfully modeled noiseless data. Implementation of this strategy requires a spatial and temporal model of the distribution of radiopharmaceutical with the SPECT field of view.

The estimation of kinetic parameters directly from projection data is potentially useful for clinical SPECT studies, particularly those which use a single detector system or body contouring orbits with a multi-detector system. Future work in this area includes incorporating additional physical factors such as scatter and geometric point response in the modeling, developing computationally efficient methods for segmenting the SPECT field of view and parametrizing non-uniform activity concentrations within the resulting ROIs, and performing weighted fits based on the covariance of the modeled projections. A weighted fit can be performed to improve the precision of the estimated kinetic parameters, or to maintain precision comparable to that obtained from an unweighted fit while reducing the patient dose.

#### V. ACKNOWLEDGMENTS

We thank Dr. EVR Di Bella for his assistance with the computer simulations, and the University of North Carolina Medical Imaging Research Laboratory for making the MCAT phantom available.

This work was supported in part by the National Heart, Lung, and Blood Institute of the U.S. Department of Health and Human Services under grants R01-HL50663 and P01-HL25840; and, in part by the Director, Office of Energy Research, Office of Biological and Environmental Research, Medical Applications and Biophysical Research Division of the U.S. Department of Energy under contract DE-AC03-76SF00098.

This work was developed in part using the computational resources at the National Energy Research Scientific Computing (NERSC) Center at Lawrence Berkeley National Laboratory.

#### VI. REFERENCES

- [1] P C Chiao, W L Rogers, N H Clinthorne, J A Fessler, and A O Hero. Model-based estimation for dynamic cardiac studies using ECT. *IEEE Trans Med Imag*, 13(2):217–226, 1994.
- [2] P C Chiao, W L Rogers, J A Fessler, N H Clinthorne, and A O Hero. Model-based estimation with boundary side information or

- boundary regularization. *IEEE Trans Med Imag*, 13(2):227–234, 1994.
- [3] M A Limber, M N Limber, A Celler, J S Barney, and J M Borwein. Direct reconstruction of functional parameters for dynamic SPECT. *IEEE Trans Nucl Sci*, 42(4):1249–1256, 1995.
- [4] G L Zeng, G T Gullberg, and R H Huesman. Using linear time-invariant system theory to estimate kinetic parameters directly from projection measurements. *IEEE Trans Nucl Sci*, 42(6):2339–2346, 1995.
- [5] R H Huesman. A new fast algorithm for the evaluation of regions of interest and statistical uncertainty in computed tomography. *Phys Med Biol*, 29(5):543–552, 1984.
- [6] M Defrise, D Townsend, and A Geissbuhler. Implementation of three-dimensional image reconstruction for multi-ring positron tomographs. *Phys Med Biol*, 35(10):1361–1372, 1990.
- [7] R E Carson. A maximum likelihood method for region-of-interest evaluation in emission tomography. *J Comput Assist Tomogr*, 10(4):654–663, 1986.
- [8] A R Formiconi. Least squares algorithm for region-of-interest evaluation in emission tomography. *IEEE Trans Med Imag*, 12(1):90–100, 1993.
- [9] R H Huesman, B W Reutter, G L Zeng, and G T Gullberg. Kinetic parameter estimation from SPECT projection measurements. *J Nucl Med*, 38(5 suppl):222P–223P, 1997. (abstract).
- [10] R H Huesman, B W Reutter, G L Zeng, and G T Gullberg. Kinetic parameter estimation from SPECT cone-beam projection measurements. *Phys Med Biol*, 43(4):973–982, 1998.
- [11] J A Terry, B M W Tsui, J R Perry, and G T Gullberg. A three-dimensional mathematical phantom of the human torso for use in SPECT imaging research studies. *J Nucl Med*, 31(5 suppl):868, 1990. (abstract).
- [12] R K Narra, T Feld, and A D Nunn. Absorbed radiation dose to humans from technetium-99m-teboroxime. *J Nucl Med*, 33(1):88–93, 1992.
- [13] A M Smith, G T Gullberg, P E Christian, and F L Datz. Kinetic modeling of teboroxime using dynamic SPECT imaging of a canine model. *J Nucl Med*, 35(3):984–995, 1994.
- [14] A M Smith, G T Gullberg, and P E Christian. Experimental verification of <sup>99m</sup>Tc-teboroxime kinetic parameters in the myocardium using dynamic SPECT: Reproducibility, correlations to flow, and susceptibility to extravascular contamination. *J Nucl Cardiol*, 3:130–142, 1996.
- [15] D M Bates and D G Watts. *Nonlinear Regression Analysis and Its Applications*. John Wiley & Sons, New York, 1988.
- [16] G A F Seber and C J Wild. *Nonlinear Regression*. John Wiley & Sons, New York, 1989.
- [17] M Kendall, A Stuart, and J K Ord. *Kendall's Advanced Theory of Statistics*, volume 1, sections 10.5–10.6. Oxford University Press, New York, 1987.
- [18] R H Huesman, G T Gullberg, W L Greenberg, and T F Budinger. Donner algorithms for reconstruction tomography. Publication PUB-214, Lawrence Berkeley Laboratory, 1977.

#### DISCLAIMER

This document was prepared as an account of work sponsored by the United States Government. While this document is believed to contain correct information, neither the United States Government nor any agency thereof, nor The Regents of the University of California, nor any of their employees, makes any warranty, express or implied, or assumes any legal responsibility for the accuracy, completeness, or

usefulness of any information, apparatus, product, or process disclosed, or represents that its use would not infringe privately owned rights. Reference herein to any specific commercial product, process, or service by its trade name, trademark, manufacturer, or otherwise, does not necessarily constitute or imply its endorsement, recommendation, or favoring by the United States Government or any agency thereof, or The Regents of the University of California. The views and opinions of authors expressed herein do not necessarily state or reflect those of the United States Government or any agency thereof, or The Regents of the University of California.

Ernest Orlando Lawrence Berkeley National Laboratory is an equal opportunity employer.